ORIGINAL RESEARCH

Comparative assessment of failure strain predictions using ductile damage criteria for warm stretch forming of IN718 alloy

Gauri Mahalle[1] · Nitin Kotkunde[1] · Amit Kumar Gupta[1] · Swadesh Kumar Singh[2]

Abstract

It is vital to envisage accurately the fracture limits of high strength superalloys when noticeable localized necking or thinning tendency is not observed during sheet-metal stretch forming process. The present study mainly focuses on fracture limits evaluation of Inconel 718 alloy (IN718) in the effective plastic strain (EPS) vs. average triaxiality space. First, uniaxial tensile test, to analyze the material properties, were instigated at different test temperatures (RT-700 °C). Subsequently, stretch forming is performed to evaluate forming and fracture forming limit diagrams (FLD and FFLD) of IN718 using Nakazima test. It is observed that forming and fractured limits of IN718 are significantly influenced by variation of processing temperatures (with approximately 65–70% improvement in major safe and fracture strains) in all deformation regions (with respect to RT). In average triaxiality (η) vs effective plastic strain (EPS) space, higher fracture limits of IN718 are noticed in the entire triaxiality path of deformation region. Seven different ductile fracture models, namely McClintock (M-Mc), Brozzo, Rice-Tracey (R-T), Ko, Oh, Cockcroft and Latham (C-L), and Clift, are formulated so as to foresee the fracture loci of IN718 in EPS vs. triaxiality space. Overall, Oh model, showed best predictability at all temperatures with least Average absolute error (AAE < 13.5%).

Introduction

Inconel 718 alloy (IN718), a Ni-Fe-Cr based precipitate-hardenable superalloy, is indispensable metal in various high temperature applications, mainly in castings of high-speed airframes, jet engine, nuclear reactor components, oil field, rocket motor, land-based gas turbine, cryogenic and pumps [1–3]. IN718 has an excellent combination of secondary precipitates into the metal matrix, which helps accomplishing an excellent combination of mechanical properties, e.g. high tensile strength, strain hardening and ductility [4, 5]. IN718 alloy is highly corrosion resistant (mostly crevice and pitting corrosion) and stable even in extreme temperature conditions [6].

The sheet metals forming process are used abundantly in manufacturing industries, specially to switch conventional welding process. Critical/complex geometry components can be manufactured easily using different forming processes. Forming of limited ductility or high strength material is very challenging. In literature, warm/elevated temperature forming is proposed as one of the proven technique to produce complex shapes of IN718 alloy. The elevated temperature forming facilitate easy flow of material in a die cavity and substantially decrease the amount of elastic recovery (springback) during the plastic deformation. But, the major issues in industrial utilities are high tooling and material cost, complex die setup, additional temperature and cooling control arrangement [7–9].

In most of the high performance/strength materials, many times, it is challenging to define the forming limit at onset of the necking, as fracture takes place without a noticeable necking in the blank specimen [10–12]. Recently, researchers considered fracture forming limit diagrams (FFLDs) to define material fracture limiting strains. These developed to evaluate the fracture limits in a minor (ε_2) and major (ε_1) strains space from uniaxial compression (T-C) to biaxial tension (T-T) region [13–17]. Basak et al. [13, 14] reported the failure strains

✉ Nitin Kotkunde
nitink@hyderabad.bits-pilani.ac.in

1 Mechanical Engineering Department, BITS Pilani -Hyderabad Campus, Hyderabad, India

2 Mechanical Engineering Department, GRIET, Hyderabad, India

of AA5052 and EDD thin sheets by FFLDs at room temperature (RT). Further, experimental strain based FLDs and FFLDs are validated with Marciniak-Kuczynski (M-K) and Bao-Wierzbicki (B-W) models. B-W fracture models show good prediction capability of all fracture strains attained for both materials. It is found that trustworthiness of these models highly depends upon reliable material properties and integration of yield criteria. Particularly at room temperature, Prasad et al. [10, 15] evaluated FFLDs for solution treated IN718 alloy. It was stated that noticeable localized necking or thinning tendency was not observed during the stretch forming process. Thus, it was proposed to predict the forming limit of IN718 alloy using FFLD only. The similar conclusions was stated by the Roamer et al. [18] for Inconel 718, 625LCF and 718SPF superalloys at room temperature.

The different proposed theoretical or semi-empirical models proposed based on necking theory may not be suitable for IN718 alloy [19, 20]. The one of the alternatives to predict the failure strains is fracture based model. Over the years, various ductile models were proposed by different researchers to envisage the material failure limits [14, 21–23]. Five different ductile fracture models, namely Cockcroft and Latham (C-L), Brozzo, Oyane and Clift models, were used to predict failure behavior by deep drawing of different grades of Aluminum alloys with computational techniques [24]. These models predicted the fracture loci and results were validated with experimental findings. Further, in numerical simulation, calculated limit drawing ratio (LDR) using above ductile models, shows good correlation with the experimental findings. Wu et al. [25] examined the fracture phenomenon with six different ductile models in hydro-piercing process. Among all six different models, Rice-Tracey (R-T) ductile model shows good prediction ability of the fracture locus. Recently, six different ductile models have been used by Prasad et al. [15] for solution treated IN718 alloy. It was observed that Oh model showed the best predictability of the fracture limits at RT.

It has been observed from the literature that failure strain prediction is highly dependent on strain paths. The dependency of failure strain prediction on strain path change can be minimized based on effective plastic strain vs. triaxiality (EPS vs. η) analysis and using stress based FLD approach [14, 21]. Bai et al. [26] evaluated sixteen different fracture models for η-EPS space and compared their accuracy on the basis of various statistical parameters for different grades of aluminum and steel alloys [27].

Based on the above studies, few reports are available on different fracture models and its implementation in failure prediction during the forming process for IN718 alloy at RT condition. Thus, the present study mainly focuses on effect of processing temperature of failure limit prediction of IN718 alloy. Further, seven different ductile fracture models are considered to predict failure locus theoretically in triaxiality (η) vs. effective plastic strain (EPS) space.

Materials and methods

IN718 alloy sheet (commercially available) of 1 mm thickness, considered in present study. Ni (51.5%), Cr (18.4%), Fe (20%), Mo (3%), Nb (5%) are major alloying elements in IN718 alloy (by weight %) with balanced other elements (Total elements ≤0.17% and each element ≤0.05%). ASTM E08/E8M-11 standards have been used to design the tensile specimen. Specimens were wire cut in 3 directions, i.e. 0°, 45° and 90° to rolling direction to determine anisotropic properties. Tensile tests were performed on a Universal Testing Machine (UTM) having 2 zone heating furnace as shown in the Fig. 1. The tests were executed at different temperatures (room temperature-700 °C) in 3 orientations with deformation rate of 2 mm/min. Average material properties have been evaluated after repeating experiment 3 times at particular test condition. Different material properties, specifically, yield and ultimate strengths, % elongation and anisotropic or Lankford coefficients, have been evaluated and are shown in Table 1. The Swift empirical equation is used to define the hardening behavior of IN718 and expressed as in Eq. 1,

$$\sigma = \left(\varepsilon + k_s \left(\varepsilon_o \right)^{n_s} \right) \tag{1}$$

where, K_s and n_s are strength coefficient and strain hardening exponent, ε_o is a strain at yield stress. Double stage strain hardening behavior was observed in case of IN718 alloy at all the temperatures. Previous studies by Mahalle et al. [28, 29] discussed in detail about hardening and flow stress behavior of IN718.

A hydraulic press with 40-Ton capacity is used to perform the stretch forming test. The hydraulic press is well equipped with an induction heating setup to perform stretch forming at high temperatures. K-type thermocouples are used to measure test temperature. Figure 2a shows the schematic diagram of the stretch forming tools setup. Six different specimen geometries were prepared as per ASTM E2218–15 standards to induce six distinct strain paths in FLD, mentioned in Fig. 2b. Hasek specimens (S4–6) were considered mainly to prevent the failure of draw bead produced by the lower width geometry [30]. In order to compute the minor and major strains after stretching test, all specimens/blanks were laser etched with circular grid (ϕ = 2.5 mm). A graphene-based lubricant, Moly-coat spray was used during stretching test. Based on the trial and error method, blank holding pressure (2.5 Bar) and punch movement (2 mm/min) were optimized for stretch forming tests at room temperature, 400 °C and 700 °C. High resolution stereo microscope equipped with an image analyzing software was used to measure minor and major diameters of stretched /deformed grid (ellipses) in stretched blanks.

Table 1   Important material properties for IN718 alloy

Temp.	σ_y(MPa)	σ_{uts}(MPa)	% elong.	ε_f	r_0	r_{45}	r_{90}	Swift Hardening law	
								Ist stage (till 0.082)	IIst stage (till 0.082)
RT	545 ± 4%	1450 ± 8%	42 ± 0.6	0.4896	0.781	0.941	1.043	$1153(\varepsilon_o + \varepsilon)^{0.1828}$	$2028(\varepsilon_o + \varepsilon)^{0.3912}$
400 °C	395 ± 5%	1101 ± 7%	49 ± 0.5	0.5221	0.997	1.095	0.969	$776(\varepsilon_o + \varepsilon)^{0.17}$	$1756(\varepsilon_o + \varepsilon)^{0.46}$
700 °C	324 ± 8%	890 ± 10%	55 ± 0.4	0.5714	1.123	1.336	1.132	$496(\varepsilon_o + \varepsilon)^{0.194}$	$1385(\varepsilon_o + \varepsilon)^{0.598}$

Where, σ_y-yield strength, σ_{uts}- Ultimate strength, % elong. - % elongation, ε_f-fracture strain, r_0, r_{45}, r_{90} -Lankford coefficients

## Forming and fracture forming limit diagrams (FLDs and FFLDs)

The stretching experiments were performed and representative fracture stretch specimens in stretch forming test are shown in the Fig. 3. FLDs using true major and minor strain values are plotted as presented in Fig. 4. The distinct colors and symbols are consigned to differentiate the safe, necking and failed ellipses in six different specimens (S1-S6). At room temperature conditions, IN718 alloy failed without a noticeable hint of the necking. Particularly in T-T region, no necking tendency has been observed. Similar results were specified by Prasad et al. [10] and Roamer et al. [18]. However, necking tendency can be identified properly at higher test temperature (700 °C) because of increase in flowablity and ductility of material. Therefore, it is not reliable to consider necking limits

to plot the FLD for this material at lower elevated temperatures. The best way to predict the forming limits of such high strength material is fracture based forming limit diagrams.

In FLD, highest major limiting strain values in T-T region, plane strain state and T-C region at RT are 0.4402, 0.374 and 0.4555 respectively. As expected, limiting true strains are rising apparently with a rise in test temperatures in the T-C, plane strain state and T-T deformation regions as presented in Fig. 5a. Visible necking points also increase with increase in temperature. Limiting true strain values perceived much higher at 700 °C than at room temperature. Maximum major safe strain values in the T-C and T-T region, are improved by 54.35% and 68.91% at 700 °C with respect to RT (Fig. 5b). The FLD slope on both sides at 700 °C increases significantly.

The bending strain effect was noticed over outer surface of specimen while enfolding around smaller

Fig. 1 Universal tensile testing machine (UTM) with magnified view of 2 zone resistance heating split furnace and tensile test specimen with different sheet orientations
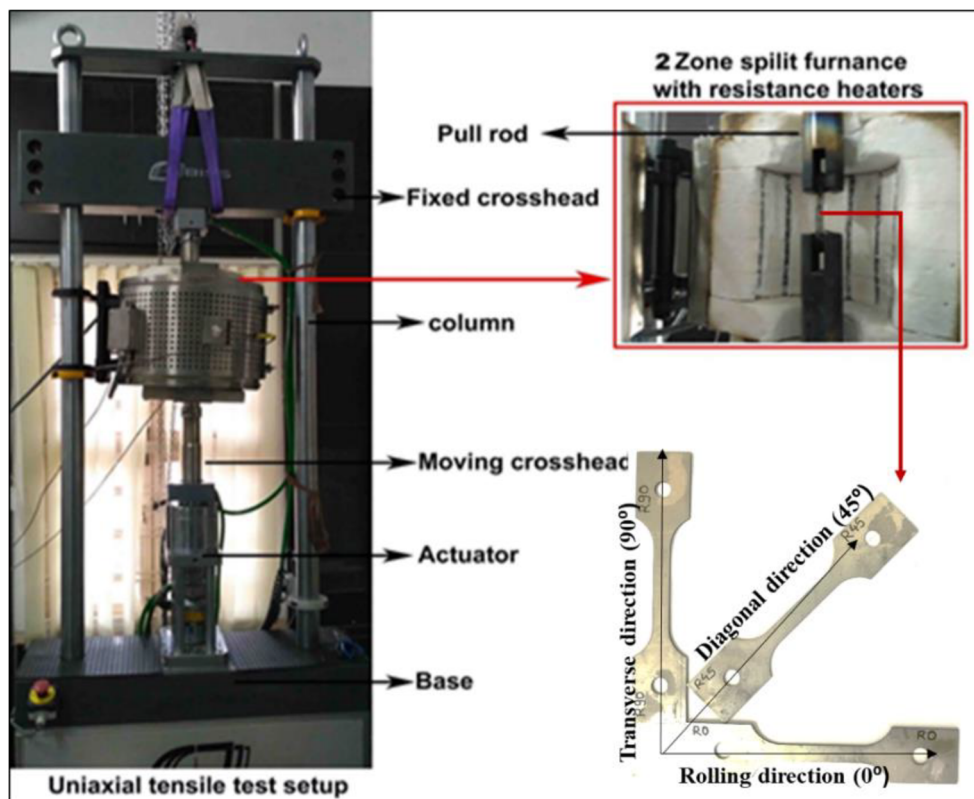
(a)

(b)
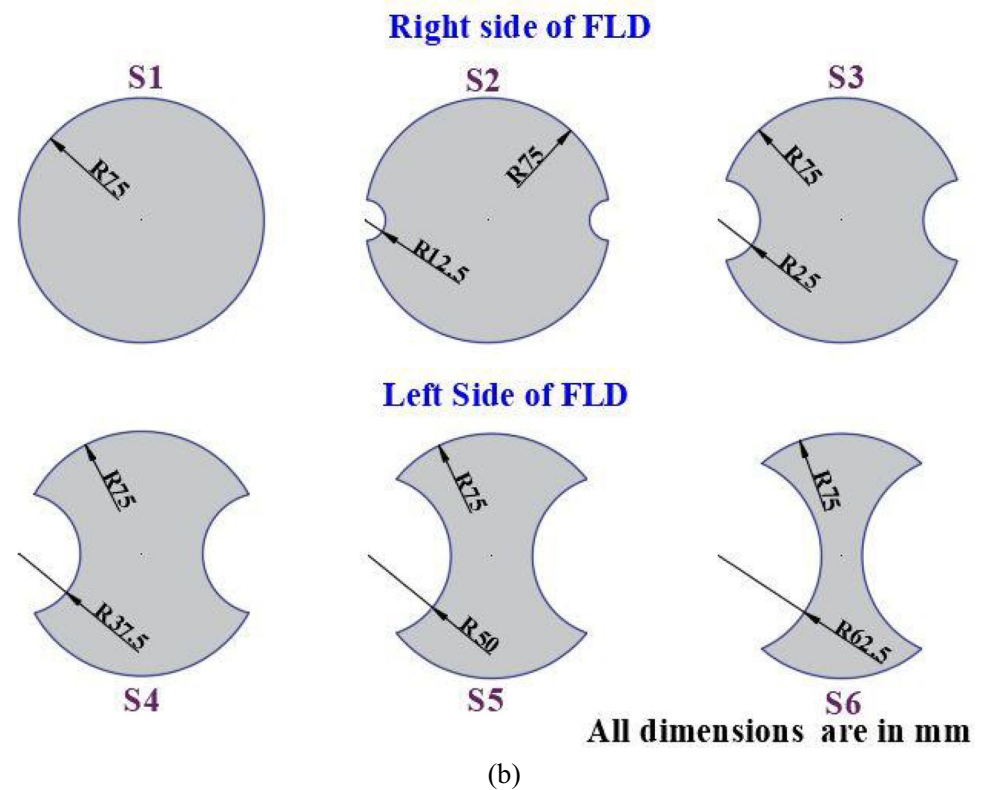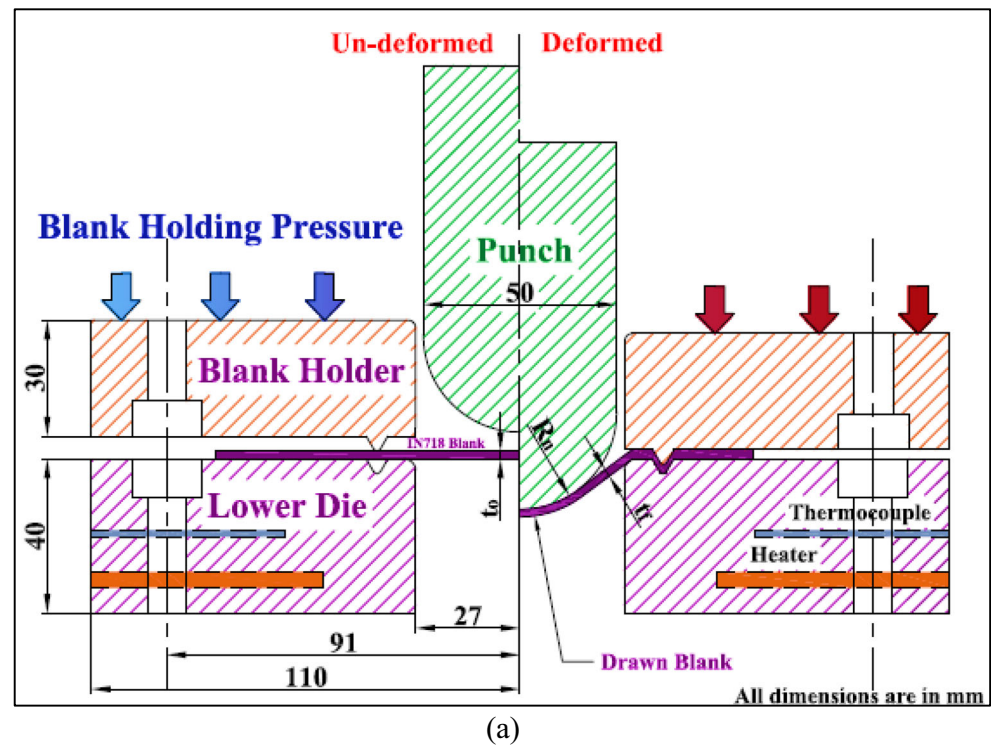
dimension punch during stretching [10]. Strain gradient
effect on the strain measurement, along the specimen
thickness, was described in the literature [30]. It was stat-
ed in literature that the FLD position is highly dependent
on the geometric factors. Specifically, punch curvature
(1/R) was directly proportional to the limiting strains
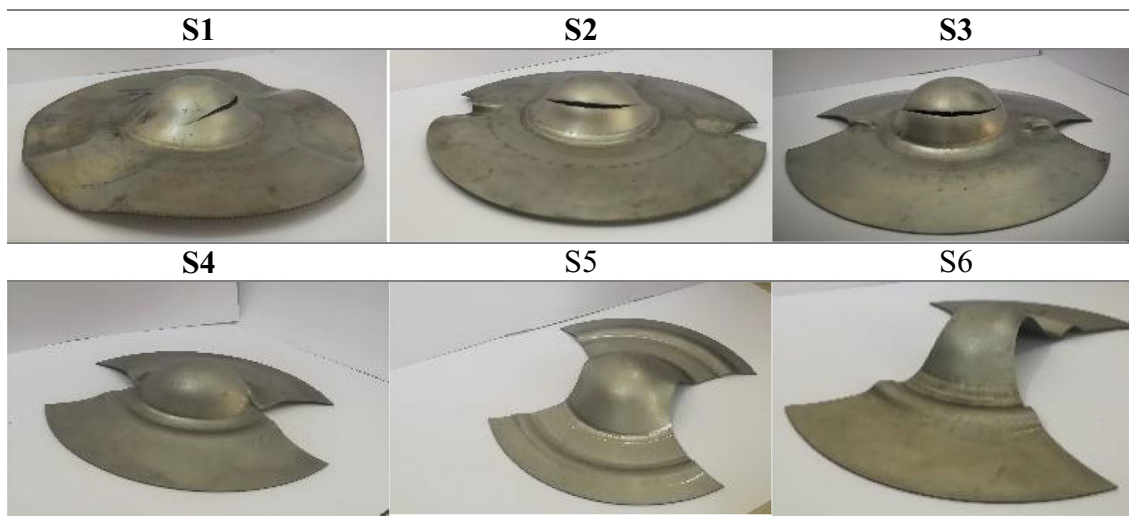when sheet thickness (t = constant) [31]. This effect is
expressed as Eq. 2.

Fig. 3 Representative stretched specimens at 400 °C for FLD prediction

$$\varepsilon_{bending} = \ln\left(1 + \frac{t_f}{2R_n}\right) \ , \text{where} t_f = t_o - \exp(-\varepsilon_1 - \varepsilon_2) \quad (2)$$

The previously measured strains or surface strains are actually a combination of bending strains and stretching strains. Thus, to measure the correct limiting strain values ($\acute{\varepsilon}_{1n, 2n}$), the measured true strains are subtracted by the induced bending strains and expressed as Eq. 3.

$$\acute{\varepsilon}_{1n,2n} = \varepsilon_{1,2} - \varepsilon_{bending} \quad (3)$$

Figure 6 shows the bending strain effect on measured FLDs. It is noted that these corrected FLDs, in all the strain regions, shifted downward approximately by 4–5% for all different test temperatures.

In Fig. 4a–c, failed ellipses (solid-color diamond symbol) on the deformed specimens does not characterize onset of fracture. So as to measure limiting strain accurately at onset of the fracture as suggested in the literature, volume constancy relation is considered, [14, 15] it is given as,

$$\varepsilon_{1f} + \varepsilon_{2f} + \varepsilon_{3f} = 0 \quad (4)$$

As considerable lateral stretching of blank specimen was not noticed after necking appears in the blank. Relatively, specimen thinning takes place through thickness direction, due to excessive strain localization. Therefore, necking strain (ε_{2n}) value and minor fracture strain (ε_{2f}) value are assumed same. Further, each fractured blank specimen is cut perpendicular to the line of the fracture. The perpendicular distances (t_{1f} & t_{2f}) from the starting of fracture edge in the maximum thinned cross-section are measured with an optical microscope. The least thickness value among (t_{1f} & t_{2f}) was considered to evaluate the true fractured thickness strain (ε_{3f}). From Eq. 4, fractured major strain value (ε_{1f}) is evaluated and the

fracture strains state is inserted in the FLDs. Multiple fracture strain points ($_{1f}$, $_{2f}$) were evaluated for an individual strain path. The square symbols (solid-colored) in Fig. 7a, characterized the onset of the fractured strain points in the deformed/stretched specimens at room temperature. A straight line, representing as FFLD, is drawn just below scattered fractured strain points in space of principal strains. Fractured strain values in FFLD increases with a rise in the test temperature in the deformation regions same as limiting strains in FLD (Fig. 7b).

Fractured strain values, at 700 °C test temperature, have been identified much higher value than that at RT because of thermal softening. % Improvement in the fractured strains with rise in temperature with respect to RT is shown in Fig. 8.

A scanning electron microscope (SEM) of Hitachi, has been used to examine fractured surfaces of fully stretched specimens. A sample (taken at fracture location from stretched specimen) has been seen parallel to the fracture surface. The sectional fractured surface of the stretched specimens (S1, S4 and S6) in T-T region, plane strain state and T-C region respectively, is shown in Fig. 9. Fractured surface has been enclosed with a large number of the equi-axed dimples, serpentine sliding characteristics and tearing edges. Existence of plenty of dimples in micrographs (Fig. 9a–k) confirms a large amount of plastic deformation due to metal matrix rupture in IN718 alloy before onset of the fracture. This concludes the high ductility of material with higher limiting strain values on left hand side of the FLD compared to that on right hand side (Fig. 4). Size of dimples and cell-like structure are fine in the nature at RT and 400 °C, whereas the rise in dimple size appear at 700 °C significantly. Because of the material softening and the diffusion healing of micro-pores, alloy shows high plasticity. This conforms the rise in limiting strains at high test temperature. In Fig. 9d–f for plane strain condition, a mixed mode fracture has been observed because of the
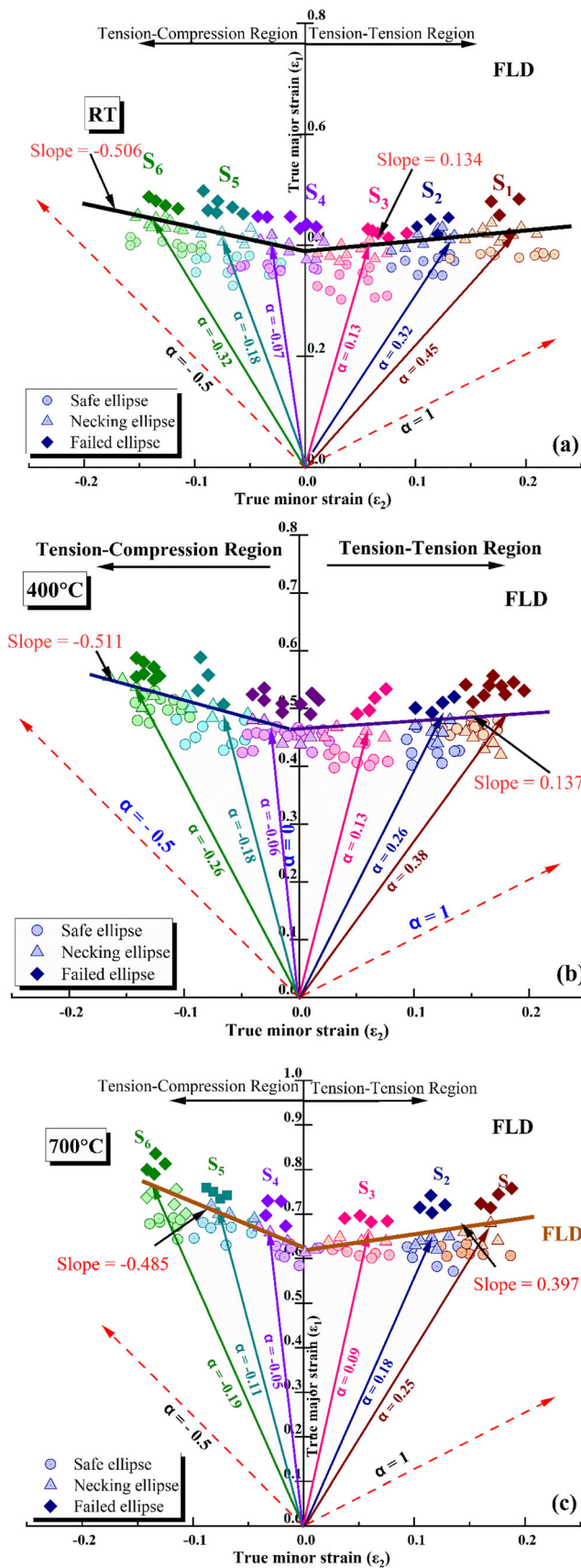
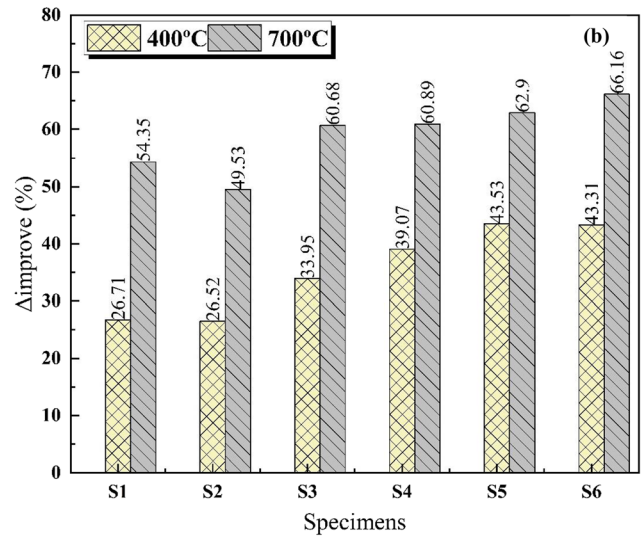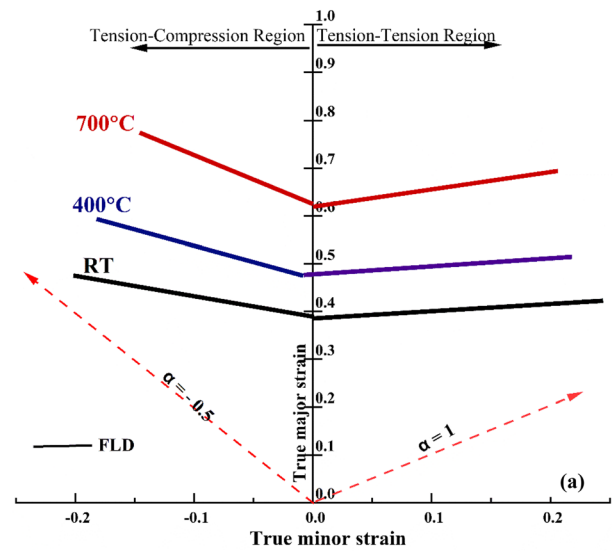Fig. 4 FLDs of IN718 at **a** RT **b** 400 °C and **c** 700 °C

Fig. 5 **a** Effect of the test temperatures on FLDs **b** % Improvement for maximum major safe strains measured for six specimens (RT values were considered as datum value)

considerable localized straining before the crack propagation. Occurrence of visible carbides at 700 °C, designates early precipitation phase of IN718 alloy. In earlier reports, it was indicated that these are precipitates or inclusions of Ni- Ti/Al/ Nb [10, 15, 32]. The noticed precipitate phases are responsible for fracture strain value improvement at 700 °C.

Theoretical fracture models

A large number of the fracture models were reported in the literature based on various experimentations, analytical and hypothesis studies for void growth [21–24, 26, 33–37]. Among all, different semi-empirical and phenomenological models, namely; McClintock (M-Mc), Brozzo et al. [15],
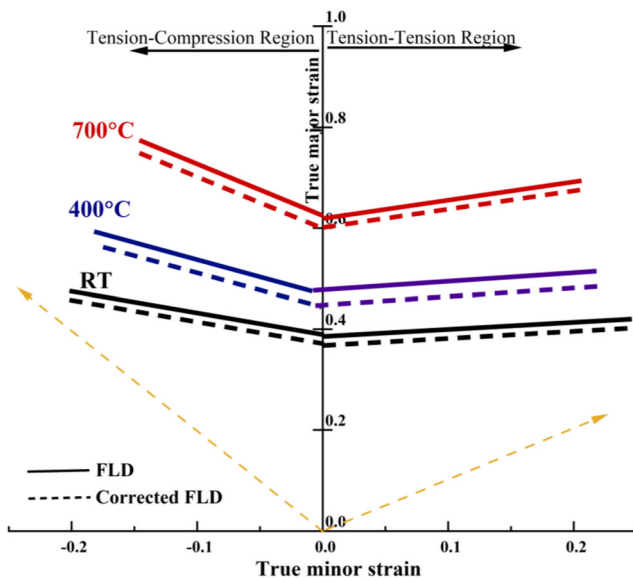
Fig. 6 Influence of bending strains on FLDs for different test temperatures

Clift et al. [36], Oh et al. [35], Rice-Tracey (R-T), Ko et al. [34] and Cockcroft-Latham (C-L), were considered for calibration of ductile fracture models in the present study. Mahalle et al. [38] observed that Barlat'89 model predict yielding behavior of IN718 alloy more accurate at different temperatures. Therefore, Barlat'89 yield function is considered in present study to define material's anisotropic behavior and expressed as in Eq. 5.

$$\overline{\sigma} = \left[\frac{1}{2}\left\{a + a|h\rho|^m + c|1-h\rho|^m\right\}\right]^{\frac{1}{m}} \times \sigma_1 \tag{5}$$

Here, a, h and c are the anisotropy functions which can be expressed by Lankford coefficient as,

$$h = \sqrt{\frac{r_0}{1+r_0} \times \frac{1+r_{90}}{r_{90}}} \tag{6}$$

$$c = 2 \times \sqrt{\frac{r_0}{1+r_0} \times \frac{r_{90}}{1+r_{90}}} \tag{7}$$

$$a = 2-c \tag{8}$$

Authors in their previous work discussed the yielding behavior by two different yield criteria, specifically Hill'48 and Barlat'89 for IN718 at elevated temperature [38]. The calculated Barlat'89 anisotropy constants are summarized in Table 2.

The associative flow law, Eq. 9, is used in Eq. 5 to determine the relationship between strain ($\alpha = \varepsilon_2/\varepsilon_1$) and stress ($\rho = \sigma_2/\sigma_1$) ratio as presented in Eq. 10.

$$d\overline{\varepsilon}_{ij} = d\lambda \frac{\partial \overline{\sigma}}{\partial \sigma_{ij}} \tag{9}$$

$$\alpha = \frac{a|h\rho|^{m-1} - ch|1-h\rho|^{m-1}}{a + c|1-h\rho|^{m-1}} \tag{10}$$

By using work per unit volume (Eq. 11) and plane stress condition, the term ξ is evaluated using Eq. 12. The term χ is evaluated using the Eq. 13.

$$dw = \sigma_1 d\varepsilon_1 + \sigma_2 d\varepsilon_2 + \sigma_3 d\varepsilon_3 = \overline{\sigma}d\overline{\varepsilon} \tag{11}$$

$$\xi = \frac{d\overline{\varepsilon}}{d\varepsilon_1} = \frac{(1 + \alpha\rho)}{\left[\frac{1}{2}\left\{a + a|h\rho|^m + c|1-h\rho|^m\right\}\right]^{\frac{1}{m}}} \tag{12}$$

$$\chi = \frac{\sigma_1}{\overline{\sigma}} = \frac{1}{\left[\frac{1}{2}\left\{a + a|h\rho|^m + c|1-h\rho|^m\right\}\right]^{\frac{1}{m}}} \tag{13}$$

The fracture prediction were studied extensively in the past by the stress triaxiality (η). It can be expressed as Eq. 14.

$$\eta = \frac{1}{3} \times \frac{(1 + \rho)}{\left[\frac{1}{2}\left\{a + a|h\rho|^m + c|1-h\rho|^m\right\}\right]^{\frac{1}{m}}} \tag{14}$$
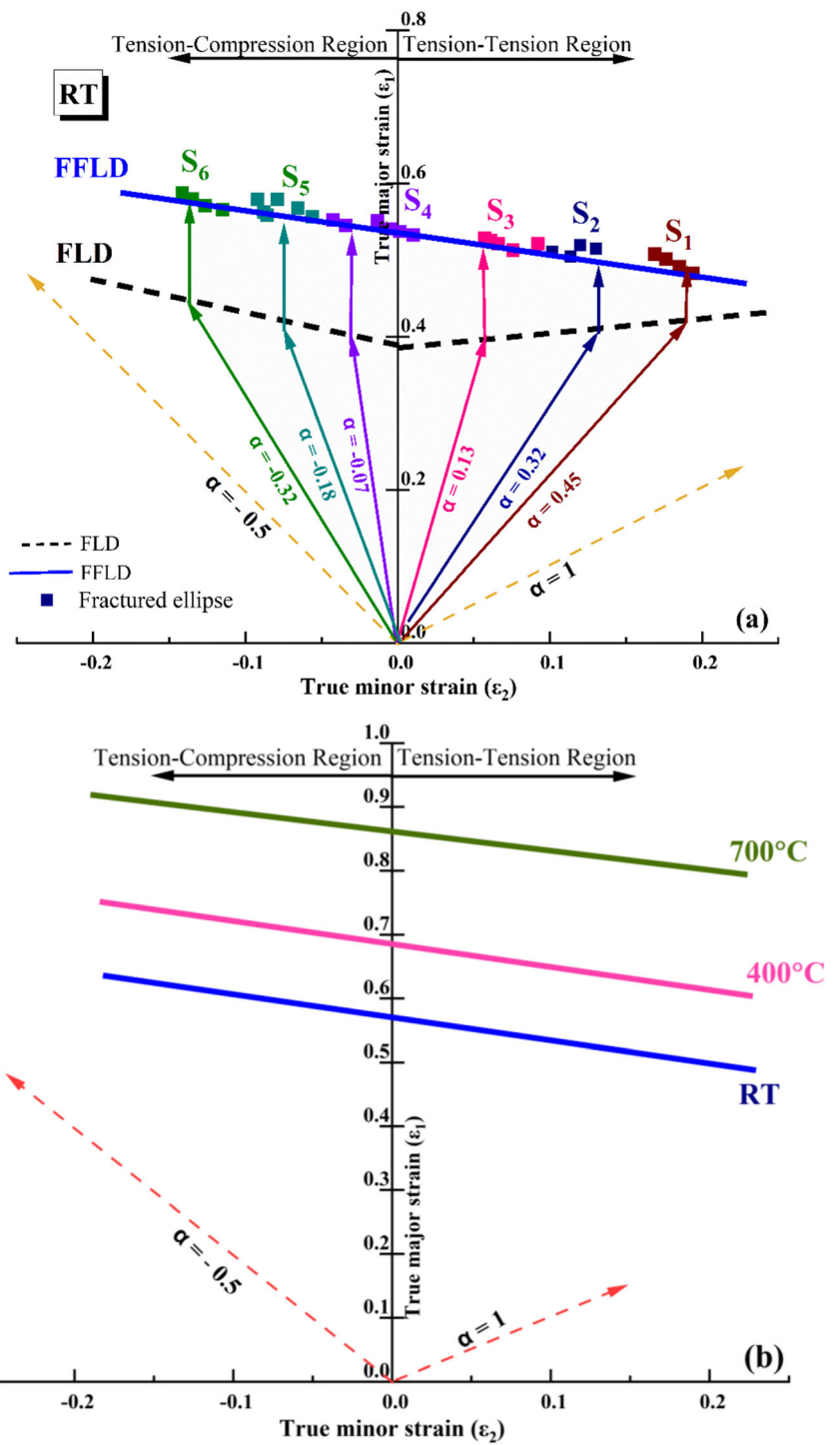
Numerous fracture models were described in the literature based on various experimentations, analytical studies and hypothesis for voids growth [22–26, 33]. Among all, some of the semi-empirical and phenomenological fracture models are deliberated for calibration of fracture coefficients in the current study.

I **McClintock (M-Mc):** M-Mc fracture model [39] prescribed the loading history over cylindrical holes and experimental results. The strain gradient effect, anisotropic and strain hardening effect on ductile fracture were studied. It is expressed mathematically as Eq. 15.

$$\int_0^{\overline{\varepsilon}_f}\left(\frac{\sigma_m}{\overline{\sigma}}\right)d\overline{\varepsilon} = \int_0^{\varepsilon_f}\left(\frac{\sigma_m}{\sigma_1} \cdot \frac{\sigma_1}{\overline{\sigma}}\right) \cdot \frac{d\overline{\varepsilon}}{d\varepsilon_1} \cdot d\varepsilon_1$$
$$= \int_0^{\varepsilon_f}\left(\frac{1+\alpha}{3}\right) \cdot \chi \cdot \xi \cdot d\varepsilon_1 = C_1 \tag{15}$$

II. **Brozzo et al. [15]:** Brozzo model includes the stress function, dependent on the maximum and mean principle stress in modified C-L criteria, as fracture strain values calculated from original C-L criteria was very small for metal. It is given as shown in Eq. 16.

Fig. 7 FFLDs for IN718 at **a** RT
and **b** Effect of test temperature
on FFLD

$$\int_{0}^{\overline{\varepsilon}_f} \frac{2\sigma_1}{3(\sigma_1 - \sigma_m)} \, d\overline{\varepsilon} = \int_{0}^{\varepsilon_f} \frac{2}{3} \cdot \frac{1}{\left(1 - \frac{\sigma_m}{\sigma_1}\right)} \cdot \frac{d\overline{\varepsilon}}{d\varepsilon_1} \cdot d\varepsilon_1$$

$$= \int_{0}^{\varepsilon_f} \frac{2}{(2-\alpha)} \cdot \xi \cdot d\varepsilon_1 = C_2 \qquad (16)$$

III. **Rice-Tracey (R-T):** R-T model [25] is a semi-empirical model. It is considered over a spherical void exists in the whole infinite solid and mainly subjected to the small amount of normal stress. It was stated that hydrostatic stress (σ_m) is more suitable to describe the void growth. Further, fracture ductility decreases rapidly with the rise in the hydrostatic stress. Fracture was characterized
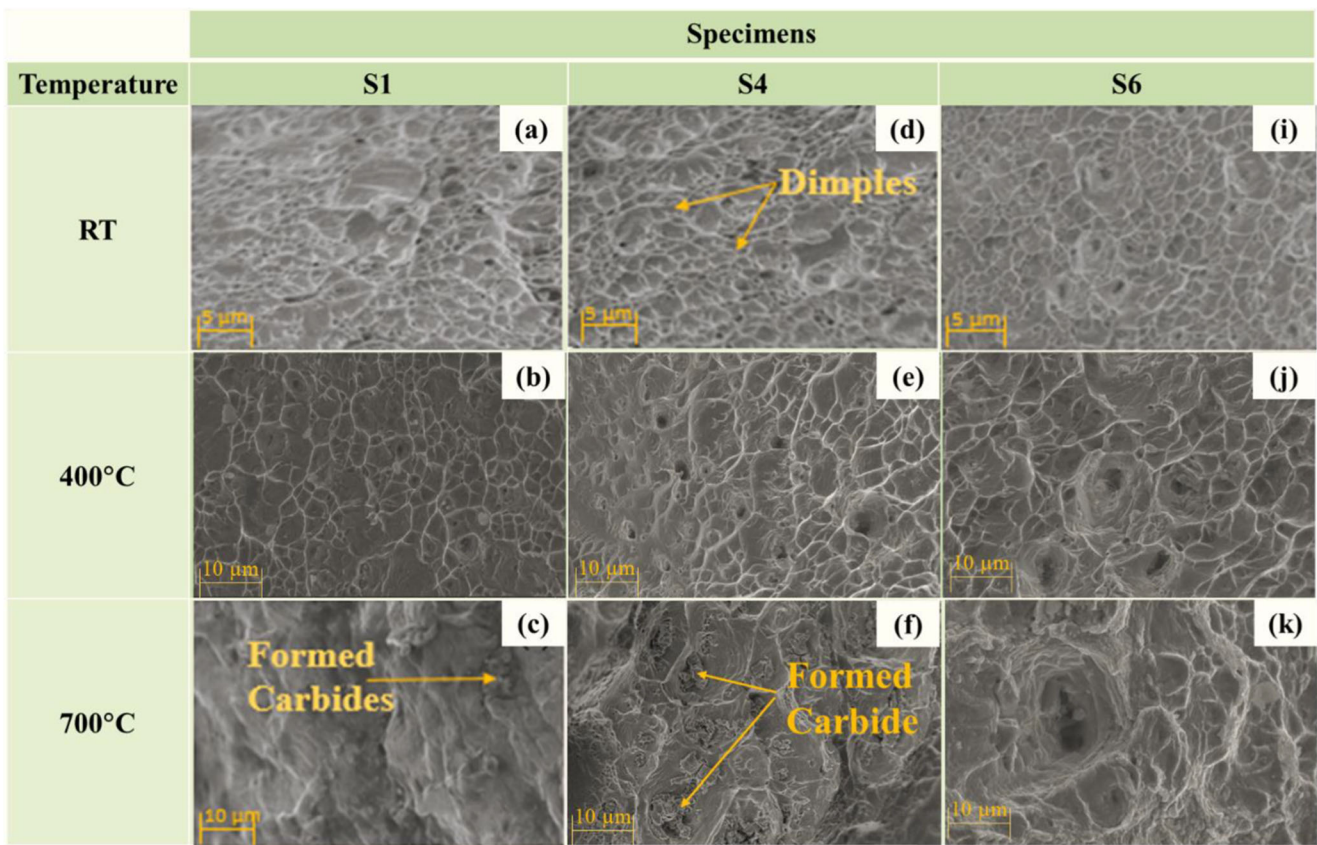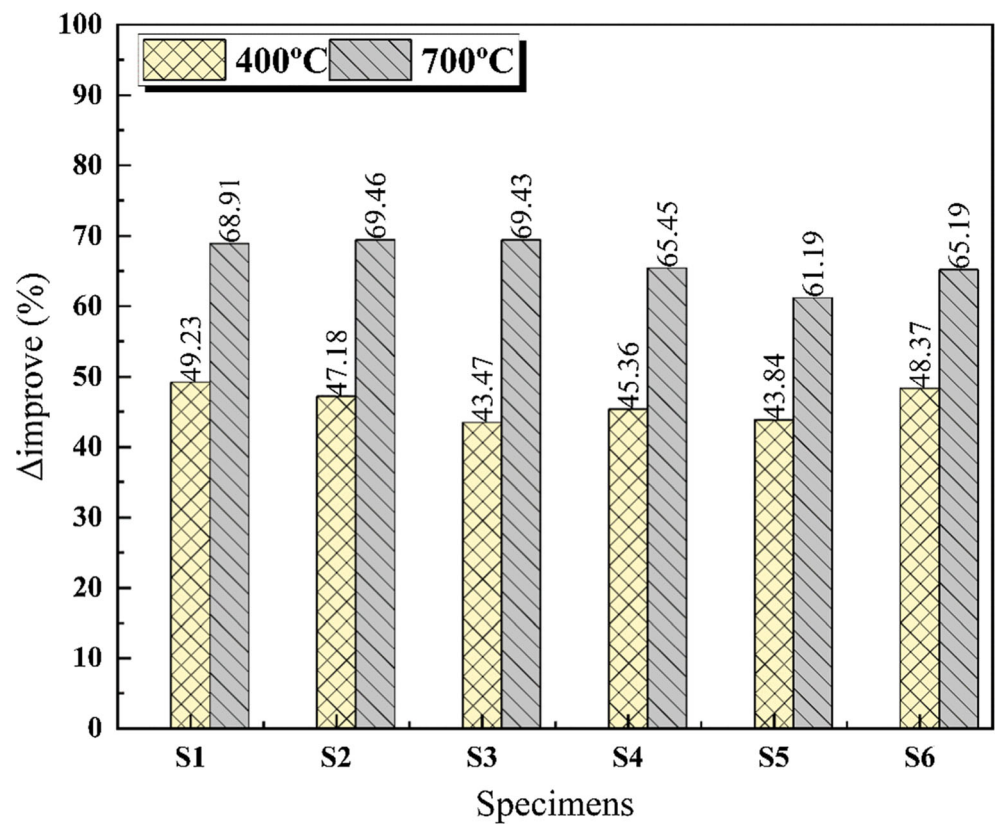
Fig. 9 Fractographs of the stretched specimens in T-T region (S1), plane strain state (S4) and T-C region (S6) at different test temperatures

Fig. 8 Improvement (%) in maximum major fracture strains measured for six different specimens (RT values were considered as datum value)

Table 2 Barlat'89 anisotropy constants at test temperatures

Temp.	a	h	c	m
RT	1.0537	0.9269	0.9463	8
400 °C	0.9871	1.0528	1.0129	8
700 °C	0.9402	0.9982	1.0598	8

using modified M-Mc model and hardening. It is mathematically expressed below by Eq. 17.

$$\int_0^{\overline{\varepsilon}_f} 0.283\, exp\left(\frac{3\sigma_m}{2\overline{\sigma}}\right) d\overline{\varepsilon} = \int_0^{\varepsilon_f} 0.283\, exp\left(\frac{3}{2}\cdot\frac{\sigma_m}{\sigma_1}\cdot\frac{\sigma_1}{\overline{\sigma}}\right)\cdot\frac{d\overline{\varepsilon}}{d\varepsilon_1}\cdot d\varepsilon_1$$
$$= \int_0^{\varepsilon_f} 0.283\, exp\left(\left(\frac{1+\alpha}{3}\right)\cdot\chi\right)\cdot\xi\cdot d\varepsilon_1 = C_3 \tag{17}$$

IV. **Ko et al. [34]:** Coupled effect of stress triaxiality and maximum principle stress to describe the material behavior in the ductile fracture was perceived by the Ko et al. [34] in original C-L criteria. It is expressed in Eq. 18.

$$\int_0^{\overline{\varepsilon}_f}\frac{\sigma_1}{\overline{\sigma}}\left(1+\frac{3\sigma_m}{\overline{\sigma}}\right)d\overline{\varepsilon} = \int_0^{\varepsilon_f}\frac{\sigma_1}{\overline{\sigma}}\cdot\left(1+3\cdot\frac{\sigma_m}{\sigma_1}\cdot\frac{\sigma_1}{\overline{\sigma}}\right)\cdot\frac{d\overline{\varepsilon}}{d\varepsilon_1}\cdot d\varepsilon_1$$
$$= \int_0^{\varepsilon_f}\chi\cdot(1+(1+\alpha)\cdot\chi)\cdot\xi\cdot d\varepsilon_1 = C_4 \tag{18}$$

V. **Oh et al. [35]:** Oh et al. [35] improved the original C-L criteria with equivalent stress to normalize the maximum principle stress. Also, it explains the material workability in metal forming processes, namely in extrusion, drawing etc. It is expressed as Eq. 19.

$$\int_0^{\overline{\varepsilon}_f}\left(\frac{\sigma_{max}}{\overline{\sigma}}\right)d\overline{\varepsilon} = \int_0^{\varepsilon_f}\left(\frac{\sigma_1}{\overline{\sigma}}\right)\cdot\frac{d\overline{\varepsilon}}{d\varepsilon_1}\cdot d\varepsilon_1 = \int_0^{\varepsilon_f}\chi\cdot\xi\cdot d\varepsilon_1 = C_5 \tag{19}$$

VI. **Cockcroft and Latham (C-L):** C-L model [37] was widely used phenomenological fracture model. It

explains 'true ductility' of the metals. It assumes that the material fracture controlled by maximum principle stress (σ_{max}). It is expressed mathematically as Eq. 20.

$$\int_0^{\overline{\varepsilon}_f}\sigma_{max}\,d\overline{\varepsilon} = \int_0^{\varepsilon_f}\frac{\sigma_1}{\overline{\sigma}}\cdot\overline{\sigma}\cdot\frac{d\overline{\varepsilon}}{d\varepsilon_1}\cdot d\varepsilon_1 = \int_0^{\varepsilon_f}\chi\cdot\overline{\sigma}\cdot\xi\cdot d\varepsilon_1 = C_6 \tag{20}$$

VII. **Clift et al. [36]:** Clift et al. [36] modified C-L criteria by assuming effect of equivalent stress over fracture of a material and is expressed in Eq. 21. According to Clift et al. the ductile fracture starts or initiates when a critical value of plastic work per unit volume is achieved.

$$\int_0^{\overline{\varepsilon}_f}\overline{\sigma}\,d\overline{\varepsilon} = \int_0^{\varepsilon_f}\overline{\sigma}\cdot\frac{d\overline{\varepsilon}}{d\varepsilon_1}\cdot d\varepsilon_1 = \int_0^{\varepsilon_f}\overline{\sigma}\cdot\xi\cdot d\varepsilon_1 = C_7 \tag{21}$$

In all above fracture models, C_{1-7} are material constants and $\overline{\varepsilon}_f$ is an equivalent plastic strain (EPS) at fracture. All these models were used to predict fracture locus and validated with experimental findings. Predictability of all above fracture models is measured by statistical parameters, specifically correlation coefficient (R), Average Absolute Error (AAE) and its standard deviation (s), expressed as,
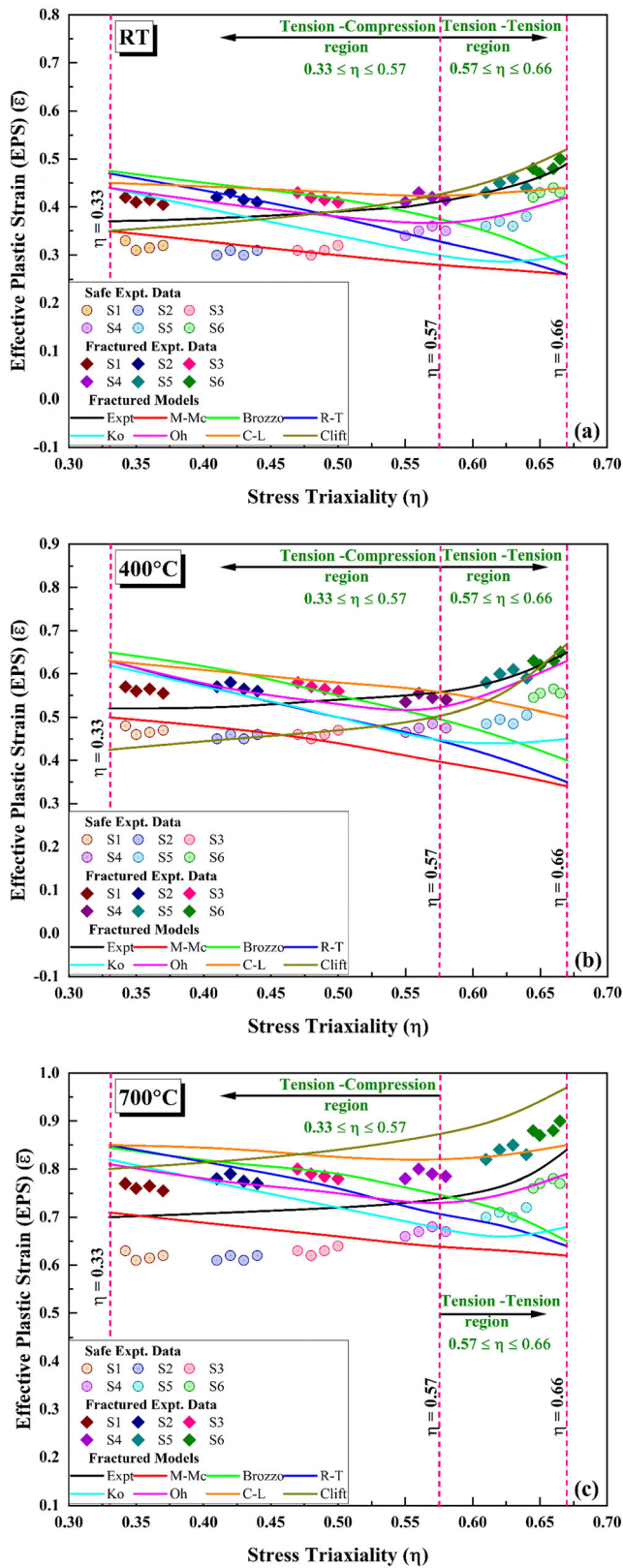
$$R = \frac{\sum_{i=1}^{N}\left(\left(\overline{\varepsilon_{f\,experimental}}\right)_i - \overline{E}\right)\left(\left(\overline{\varepsilon_{f\,predicted}}\right)_i - \overline{P}\right)}{\sqrt{\sum_i^N\left(\left(\overline{\varepsilon_{f\,experimental}}\right)_i - \overline{E}\right)^2\left(\left(\overline{\varepsilon_{f\,predicted}}\right)_i - \overline{P}\right)}}$$

$$\text{AAE}\,(\Delta avg) = \frac{1}{N}\sum_{i=1}^{N}\left|\frac{\left(\overline{\varepsilon_{f\,experimental}}\right)_i - \left(\overline{\varepsilon_{f\,predicted}}\right)_i}{\left(\overline{\varepsilon_{f\,experimental}}\right)_i}\right|$$

$$s = \sqrt{\frac{\sum_i^N\left(\left(\overline{\varepsilon_{f\,experimental}}\right)_i - \left(\overline{\varepsilon_{f\,predicted}}\right)_i\right)^2}{N}} \tag{22}$$

Table 3 Calibrated fracture model parameters for IN718 alloy at different temperatures

| Calibrated fracture models	Damage parameters	Temperature		
		RT	400 °C	700 °C
McClintock	C_1	0.2666	0.3221	0.3876
Brozzo	C_2	0.6635	0.7544	0.8905
Rice-Tracey	C_3	0.2348	0.2823	0.3325
Ko	C_4	1.3956	1.7509	2.1093
Oh	C_5	0.5146	0.6436	0.7498
Cockcroft and Latham	C_6	294.613	212.187	208.368
Clift	C_7	269.039	185.622	178.613

Fig. 10 Fracture loci predicted by seven different fracture models with experimental data at **a** RT, **b** 400 °C, **c** 700 °C in average stress triaxiality (η) -EPS space

Here, $\overline{\varepsilon_{f\,experimental}}$ and $\overline{\varepsilon_{f\,predicted}}$ are experimental and predicted fracture equivalent plastic strain. N is total number of the considered points in analysis. $\overline{E}$ & $\overline{P}$ represent mean values of $\overline{\varepsilon_{f\,experimental}}$ and $\overline{\varepsilon_{f\,predicted}}$ respectively. Experimental fracture limits of IN718 alloy are considered as reference to check prediction accuracy of all above models.

Calibration of fracture models

Experimentally calculated strains corresponding to the failure along different strain paths are transformed into EPS and effective stress $\overline{\sigma}$ using Eq. 1. Calculated effective stress $\overline{\sigma}$ is
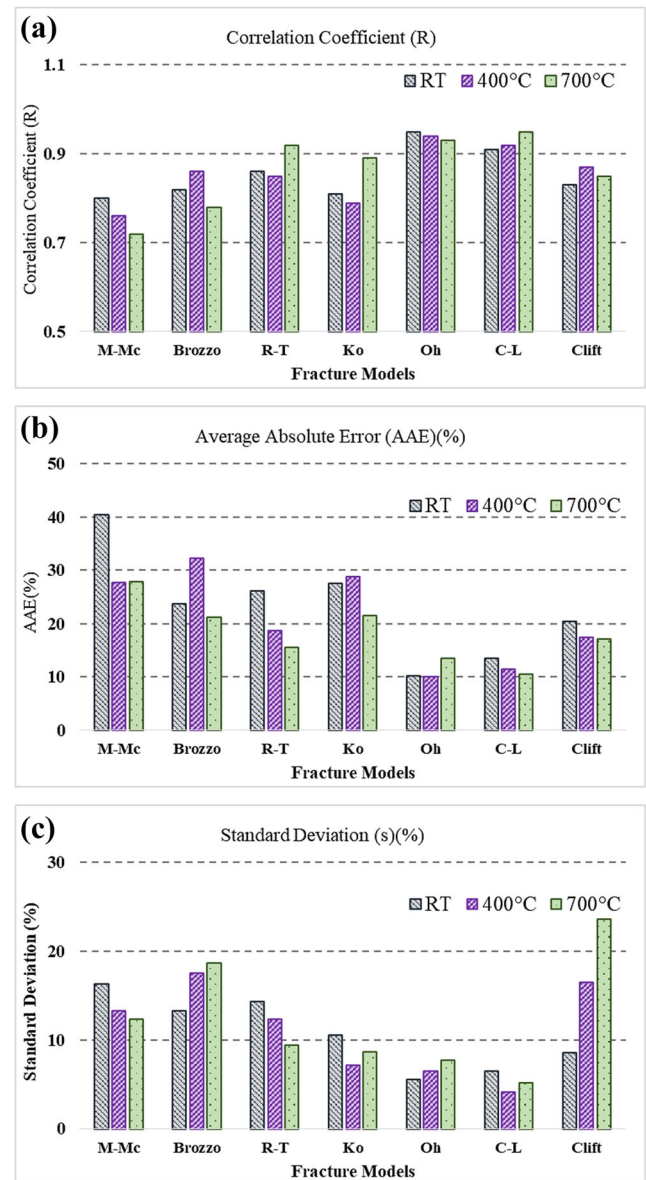
Fig. 11 Deviation of models in terms of statistical parameters w.r.t. the experimental values

used to convert the effective stress into true major and minor stresses with Eq. 13 and stress ratio (ρ). Then finally stress triaxiality (η) is calculated from these stress components. To get fracture locus, EPS vs. η is plotted. Damage parameters, at different test temperatures for seven different fracture models studied in present study, are mentioned in Table 3. Figure 10 gives the fracture loci drawn using seven different ductile fracture models in the EPS vs. average stress triaxiality (η) space of IN718 alloy at different test temperatures.

It is noticed that fracture limits of IN718 alloy are higher in the entire triaxiality path ($0.33 < η < 0.66$ approximately) of the deformation region (from T-C to T-T region). Prasad et al. [15] reported that these high values of EPS to fracture is due to decrease in secondary precipitates of Ni- Nb /Ti/Al phases (i.e. $γ′$ and $γ″$), which ultimately delay void nucleation and improve EPS to fracture occurrence. It is noted that all studied models show deviation from experimental fracture locus. For RT, all fracture models over-predicted, except M-Mc model in the T-C region, this indicates the locus follow the experimental curve approximately. However, most of the fracture models in T-T region under-predicted experimental path except Clift criterion. While at 400 °C and 700 °C, M-Mc model only appears to under-predict the locus in the T-C region. As, predicted curves are deviated in the whole triaxiality region for all the fracture models. Hence, nothing particular can be concluded for the under and over predictability of the fracture loci.

This variation is noted along different triaxiality paths in the range of $0.33 ≤ η ≤ 0.66$. It is observed that the triaxiality variation of curve in the T-T region is more compared to one in T-C region. Higher EPS values have been perceived in the T-T region (higher triaxiality space) for all test temperatures. To have a clear understanding, prediction capability of all these considered models is evaluated, by Eq. 22, based on various statistical parameters like a correlation coefficient, standard deviation (s) and average absolute error AAE (Δ), as presented in Fig. 11.

First, quantifying tool, correlation coefficient (R) has been used for all test temperatures. The prediction capability of all chosen model was evaluated based on correlation coefficient (R) as shown in Fig. 11a. At RT, the correlation coefficient was minimum for M-Mc fracture model ($R < 0.7924$) with respect to the experimental values. Even at high temperature, M-Mc model displays poor correlation coefficient (R) in all other fracture models. Among all other fracture models, Oh and C-L fracture models show better and comparable correlation coefficient with 0.95 and 0.92 respectively at RT. As, correlation coefficient (R) is a biased parameter and its values might be biased towards lower or higher values [40, 41], additional statistical parameters, namely the standard deviation (s) and average absolute error AAE (Δ) are need to be consider for comparison.

Thus, the next quantifying tool for the error, AAE has been used for all test temperatures. The prediction capability of all

these chosen model on average absolute error AAE (%) as shown in Fig. 11b. Oh criterion at RT, shows minimum error (10.2%) with respect to experimental results. C-L and Clift fracture model also exhibited a good correlation with AAE as 13.6% and 20.4% respectively. M-Mc fracture model displayed worst predictability with AAE as 40.4%. Even at 400 °C, Oh model showed good predictability with least AAE value of 10.1%. Other fracture models, namely, R-T, C-L, and Clift models, predict fracture locus well, but highest AAE of 32.3% is displayed by Brozzo model. Hence, this model is not suitable to predict fracture limits for IN718 alloy at 400 °C. Whereas at 700 °C, least AAE of 10.5% is displayed by C-L model followed by the Oh (13.5%), R-T (15.6%) and Clift (18.52%) models. Highest AAE of 27.8% is by M-Mc model at 700 °C, thus it is less suitable for the fracture locus prediction.

Further, Fig. 11c gives the prediction capability of all these selected models based on its standard deviation (s). It is observed that Oh fracture model shows least standard deviation (5.49%) at RT, whereas C-L model shows least deviation (5.18%) at 700 °C. Even at 400 °C, Oh and C-L fracture models show better predictability with least standard deviation as 6.4% and 4.08% respectively.

By considering the variation of statistical parameters, Oh model is best suitable at RT and C-L model is better at 700 °C to predict the fracture locus for IN718 alloy. Whereas either of the models can be used to predict locus at 400 °C. Overall, Oh model, which defines the material workability in forming processes, can be used to predict fracture locus at test temperatures for high accuracy. This might be due to high workability of Inconel alloy until 700 °C. The detailed discussion, on hot workability using processing maps for IN718 alloy, was described in previous studies [5]. Prasad et al. [15] also reported that Oh model has highest fracture locus prediction capability for IN718 alloy at RT.

Conclusion

In the present study, failure prediction of IN718 alloy is studied by damage modeling technique for different test temperatures. Based on the results, important conclusions are drawn as:

i   Experimental forming limits of IN718 alloy are significantly influenced by variation of processing temperatures. Maximum major safe strain values in the T-C and T-T region, are improved by 54.35% and 68.91% at 700 °C with respect to RT. The bending strain effect is analyzed and forming limit diagrams (FLDs) are corrected based on bending correction factor. These corrected FLDs, in all the strain regions, shifted downward approximately by 4–5%.

j Fractured forming limit diagrams (FFLDs) for IN718 alloy at different test temperature is also evaluated and significantly influenced by test temperatures. FFLDs is transferred to triaxiality (η) vs effective plastic strain (EPS) locus. Fracture limits of IN718 alloy is higher in the entire triaxiality path ($0.33 < \eta < 0.66$ approximately) of the deformation region.

k Seven different ductile models were imposed to predict the fracture loci in EPS vs. average stress triaxiality (η) space at different test temperatures. It was observed that the Oh model exhibited best prediction capability at RT and 400 °C with AAE of 10.2% and 10.1% respectively. Whereas, C-L model best prediction of fracture locus at 700 °C with AAE as 10.5%. Overall, Oh model can be used to predict fracture locus with high accuracy for all test temperatures.

Future work includes implementation of considered ductile fracture model in the FE analysis for failure strain prediction.

Data Availability Not applicable.

Compliance with ethical standards

Conflict of interest/Competing interest No Conflict of interest

Code availability Not applicable.

References

1. Schafrik RE, Ward DD, Groh JR (2001) Application of alloy 718 in GE aircraft engines: past, present and next five years. In: Superalloys 718, 625, 706 and various derivatives

2. Lawrence H. Thaller AHZ (2003) Overview of the design, development, and application of nickel-hydrogen batteries, NASA Tech. National Aeronautics and Space Administration, Glenn Research Center

3. Mahalle G, Kotkunde N, Kumar Gupta A, Kumar Singh S (2018) Study of mechanical properties and microstructural analysis for inconel alloy sheet at elevated temperature. Mater Today Proc 5(9):18016–18023. https://doi.org/10.1016/j.matpr.2018.06.135

4. Thomas A, El-Wahabi M, Cabrera JM, Prado JM (2006) High temperature deformation of Inconel 718. J Mater Process Technol 177(1-3):469–472. https://doi.org/10.1016/j.jmatprotec.2006.04.072

5. Mahalle G, Kotkunde N, Gupta AK, Singh SK (2019) Analysis of hot workability of Inconel alloys using processing maps. In: Advances in computational methods in manufacturing. Springer, pp 109–118

6. Reed RC (2006) The Superalloys fundamentals and applications. Cambridge University Press, New York

7. Panicker SS, Singh HG, Panda SK, Dashwood R (2015) Characterization of tensile properties, limiting strains, and deep drawing behavior of AA5754-H22 sheet at elevated temperature. J Mater Eng Perform 24(11):4267–4282. https://doi.org/10.1007/s11665-015-1740-6

8. Kotkunde N, Badrish A, Morchhale A, Takalkar P, Singh SK (2019) Warm deep drawing behavior of Inconel 625 alloy using constitutive modelling and anisotropic yield criteria. Int J Mater Form 13(3):1–15. https://doi.org/10.1007/s12289-019-01505-3

9. Badrish CA, Kotkunde N, Mahalle G, Singh SK, Mahesh K (2019) Analysis of hot anisotropic tensile flow stress and strain hardening behavior for Inconel 625 alloy. J Mater Eng Perform 28(12):7537–7553. https://doi.org/10.1007/s11665-019-04475-4

10. Prasad SK, Panda SK, Kar SK et al (2017) Microstructures, forming limit and failure analyses of Inconel 718 sheets for fabrication of aerospace components. J Mater Eng Perform 26(4):1513–1530. https://doi.org/10.1007/s11665-017-2547-4

11. Jafarian F, Masoudi S, Soleimani H, Umbrello D (2018) Experimental and numerical investigation of thermal loads in Inocnel 718 machining. Mater Manuf Process 23(9):1020–1029. https://doi.org/10.1080/10426914.2018.1424907

12. Kuroda M, Tvergaard V (2000) Forming limit diagrams for anisotropic metal sheets with different yield criteria. Int J Solids Struct 37(37):5037–5059. https://doi.org/10.1016/S0020-7683(99)00200-0

13. Basak S, Panda SK (2019) Failure strains of anisotropic thin sheet metals: experimental evaluation and theoretical prediction. Int J Mech Sci 151:356–374. https://doi.org/10.1016/j.ijmecsci.2018.10.065

14. Basak S, Panda SK, Zhou YN (2015) Formability assessment of prestrained automotive grade steel sheets using stress based and polar effective plastic strain-forming limit diagram. J Eng Mater Technol Trans ASME 137(4):1–12. https://doi.org/10.1115/1.4030786

15. Prasad KS, Panda SK, Kar SK, Murty SVSN, Sharma SC (2018) Prediction of fracture and deep drawing behavior of solution treated Inconel-718 sheets: numerical modeling and experimental validation. Mater Sci Eng A 733:393–407. https://doi.org/10.1016/j.msea.2018.07.007

16. Bruschi S, Altan T, Banabic D, Bariani PF, Brosius A, Cao J, Ghiotti A, Khraisheh M, Merklein M, Tekkaya AE (2014) Testing and modelling of material behaviour and formability in sheet metal forming. CIRP Ann Manuf Technol 63(2):727–749. https://doi.org/10.1016/j.cirp.2014.05.005

17. Güler B, Efe M (2018) Forming and fracture limits of sheet metals deforming without a local neck. J Mater Process Technol 252:477–484. https://doi.org/10.1016/j.jmatprotec.2017.10.004

18. Roamer P, Van Tyne CJ, Matlock DK et al (1997) Room temperature formability of alloys 625LCF, 718 and 718SPF. Miner Met Mater Soc:315–329. https://doi.org/10.7449/1997/superalloys_1997_315_329

19. Dilmec M, Halkaci HS, Ozturk F, Livatyali H, Yigit O (2013) Effects of sheet thickness and anisotropy on forming limit curves of AA2024-T4. Int J Adv Manuf Technol 67(9-12):2689–2700. https://doi.org/10.1007/s00170-012-4684-0

20. Banabic D (2010) A review on recent developments of Marciniak-Kuczynski model. Comput Methods Mater Sci 10:225–237

21. Bao Y, Wierzbicki T (2004) On fracture locus in the equivalent strain and stress triaxiality space. Int J Mech Sci 46(1):81–98. https://doi.org/10.1016/j.ijmecsci.2004.02.006

22. Isik K, Silva MB, Tekkaya AE, Martins PAF (2014) Formability limits by fracture in sheet metal forming. J Mater Process Technol 214(8):1557–1565. https://doi.org/10.1016/j.jmatprotec.2014.02.026

23. Park N, Huh H, Lim SJ, Lou Y, Kang YS, Seo MH (2017) Fracture-based forming limit criteria for anisotropic materials in sheet metal forming. Int J Plast 96:1–35. https://doi.org/10.1016/j.ijplas.2016.04.014

24. Takuda H, Mori K, Hatta N (1999) The application of some criteria for ductile fracture to the prediction of the forming limit of sheet metals. J Mater Process Technol 95(1-3):116–121. https://doi.org/10.1016/S0924-0136(99)00275-7

25. Wu Z, Li S, Zhang W, Wang W (2010) Ductile fracture simulation of hydropiercing process based on various criteria in 3D modeling. Mater Des 31(8):3661–3671. https://doi.org/10.1016/j.matdes.2010.02.046

26. Bai Y, Wierzbicki T (2015) A comparative study of three groups of ductile fracture loci in the 3D space. Eng Fract Mech 135:147–167. https://doi.org/10.1016/j.engfracmech.2014.12.023

27. Bai Y, Teng X (2009) On the application of stress triaxiality formula for plane strain fracture testing. J Eng Mater Technol 131(2):1–10. https://doi.org/10.1115/1.3078390

28. Mahalle G, Salunke O, Kotkunde N, Gupta AK, Singh SK (2019) Neural network modeling for anisotropicmechanical properties and work hardeningbehavior of Inconel 718 alloy at elevatedtemperatures. J Mater Res Technol 8(2):2130–2140. https://doi.org/10.1016/j.jmrt.2019.01.019

29. Mahalle G, Kotkunde N, Gupta AK, Sujith R, Singh SK, Lin YC (2019) Microstructure characteristics and comparative analysis of constitutive models for flow stress prediction of Inconel 718 alloy. J Mater Eng Perform 28(6):3321–3321. https://doi.org/10.1007/s11665-019-04116-w

30. Hecker SS (1975) Simple technique for determining forming limit curves. Sheet Met Ind 52:671–676

31. Charpentier PL (1975) Influence of punch curvature on the stretching limits of sheet steel. Metall Trans A 6(8):1665–1669. https://doi.org/10.1007/BF02641986

32. Mahalle G, Morchhale A, Kotkunde N, Gupta AK, Singh SK, Lin YC (2020) Forming and fracture limits of IN718 alloy at elevated temperatures: experimental and theoretical investigation. J Manuf Process 56:482–499. https://doi.org/10.1016/j.jmapro.2020.04.070

33. Cheng C, Meng B, Han JQ, Wan M, Wu XD, Zhao R (2017) A modified Lou-Huh model for characterization of ductile fracture of DP590 sheet. Mater Des 118:89–98. https://doi.org/10.1016/j.matdes.2017.01.030

34. Ko YK, Lee JS, Huh H, Kim HK, Park SH (2007) Prediction of fracture in hub-hole expanding process using a new ductile fracture criterion. J Mater Process Technol 187–188:358–371. https://doi.org/10.1016/j.jmatprotec.2006.11.071

35. Oh SI, Chen CC, Kobayashi S (1979) Ductile fracture in axisymmetric extrusion and drawing: part 2 workability in extrusion and drawing. J Manuf Sci Eng Trans ASME 101(1):36–44. https://doi.org/10.1115/1.3439471

36. Clift SE, Hartley P, Sturgess CEN, Rowe GW (1990) Fracture prediction in plastic deformation processes. Int J Mech Sci 32(1):1–17. https://doi.org/10.1016/0020-7403(90)90148-C

37. Cockcroft MG, Lathan DJ (1968) Ductility and the workability of metals. In: J. Inst. Met. https://books.google.co.in/books/about/Ductility_and_the_Workability_of_Metals.html?id=COSPAQAACAAJ&redir_esc=y. Accessed 18 Oct 2019

38. Mahalle G, Salunke O, Kotkunde N et al (2019) Anisotropic yielding behaviour of Inconel 718 alloy at elevated temperatures. In: ASME international mechanical engineering congress and exposition, proceedings (IMECE2019). Salt Lake City, Utah, USA, pp 1–5

39. McClintock FA (1964) A criterion for ductile fracture by the growth of holes. J Appl Mech Trans ASME 35(2):363–371. https://doi.org/10.1115/1.3601204

40. Samantaray D, Mandal S, Bhaduri AK (2009) A comparative study on Johnson cook, modified Zerilli-Armstrong and Arrhenius-type constitutive models to predict elevated temperature flow behaviour in modified 9Cr-1Mo steel. Comput Mater Sci 47(2):568–576. https://doi.org/10.1016/j.commatsci.2009.09.025

41. Che J, Zhou T, Liang Z, Wu J, Wang X (2018) An integrated Johnson–cook and Zerilli–Armstrong model for material flow behavior of Ti–6Al–4V at high strain rate and elevated temperature. J Brazilian Soc Mech Sci Eng 40(5):1–10. https://doi.org/10.1007/s40430-018-1168-7